



Photocatalytic Degradation of Phenol Red by Using New Spinel-Type $\text{Co}_{1-x}\text{Cd}_x\text{Fe}_2\text{O}_4$ Nanocomposites

ASSEL A. HADI* and NADA Y. FAIROOZ

Department of Chemistry, College of Science, University of Babylon, Hilla, Iraq

*Corresponding author: E-mail: zozo_assel@yahoo.com

Received: 16 May 2018;

Accepted: 6 July 2018;

Published online: 27 September 2018;

AJC-19094

The investigation of synthesis of the spinel $\text{Co}_{1-x}\text{Cd}_x\text{Fe}_2\text{O}_4$ photocatalyst by co-precipitation method at various proportions of ($x = 0.2:0.8, 0.5:0.5, 0.8:0.2$) and calcinations at temperature 600°C for 3 h. The synthesized powder was characterized by X-ray diffraction, FT-IR, UV-visible spectroscopy, SEM, EDS, AFM and HPLC. The photocatalytic activity was estimated under high pressure mercury lamp OSRAM (125) watts for degradation phenol red solution at the wavelength of $\lambda_{\text{max}} 432 \text{ nm}$. The conclusion demonstrated that (0.5:0.5) rate at 600°C has high action than other proportion at various temperature. After this examination, a few measures, for example, better of mass for the catalyst, initial of concentration for spinel $\text{Co}_{1-x}\text{Cd}_x\text{Fe}_2\text{O}_4$, effect of pH and effect of temperature. The X-ray and electron microscopy studies showed an average size of the granules prepared for the composite in this manner (18.16-39.64). The electrical characteristics (L.C.R) were additionally examined for all the spinels. Cadmium alone was an electrical insulator but by adding cobalt with iron it turned into a semiconductor of an electric current.

Keywords: Photocatalytic degradation, Phenol red, Co-precipitation method, Nanocomposite.

INTRODUCTION

Nanosized spinel ferrite particles, an example of delicate magnetic materials with basic formula $\text{CoCdFe}_2\text{O}_4$. It is considered one of the most important committed transition metal oxides (TMO) for pseudo-capacitive energy storage. On account of the most drawing in class of materials appropriate to their pleasant and critical properties, for example, low-liquefying point, high particular heating, large development coefficient, low immersion magnetic moment and low magnetic progress temperature [1,2]. Remarkable electrical and magnetic properties of ferrites comprise upon the nature of the ions, here changes and their dispersion among tetrahedral and octahedral geometries [3-5].

A ferrite is a substance compound of earthen ware materials with iron(III) oxide (Fe_2O_3) as its principal part. Ferrites are typically non-conductive ferrimagnetic earthen ware mixes got from iron oxides, for example, hematite (Fe_2O_3) or magnetite (Fe_3O_4) as well as oxides of other metals. Nanotechnology is one of the fundamental logical fields today since it gathers between learning from the fields of chemistry, physics, biology,

engineering and medicine. The implementation and utilization of nanomaterials are wide, for example, in electronic and mechanical gadgets, optical magnetic part, tissue designing magnetic stockpiling frameworks and magnetic bounce back imaging [6,7].

Nanotechnology and material innovation are new system for synthesis and treatment manipulation and organization utilizing natures have structure prevent (atoms, particles or large scale atoms) for the clever design of practical materials, components and regulation with alluring characteristics and capacities [8,9]. Ferrites are notable magnetic nanomaterials contemplated as a documentation media appropriate to their excellent physical properties. These properties make ferrites a typical contender for technical applications, for example, magnetic reverberation imaging upgrade, catalysis, sensors and pigments [10]. Mixed spinel ferrites have been considered widely out of the most recent couple of years because of their plausibility applications. Spinel ferrites have the compound formula $\text{Co}_{1-x}\text{Cd}_x\text{Fe}_2\text{O}_4$. In spinel ferrite, oxygen shapes confront focus cubic lattice with divalent cations at tetrahedral and octahedral position. Cobalt ferrite (CoFe_2O_4) has an opposite spinel structure with the preference of Co^{2+} for the most part on octahedral

position [11-14], while cadmium ferrite (CdFe_2O_4) has simple spinel structure, in which Co^{2+} mainly occupy tetrahedral position [11,15].

In this work, $\text{Co}_{1-x}\text{Cd}_x\text{Fe}_2\text{O}_4$ nanoferrites where ($x = 0.0, 0.2, 0.5$ and 0.8) were synthesized using co-precipitation methods. X-ray diffraction (XRD) was utilized as a part of request to research the basic of Cd substituted cadmium nanoferrites and to decide the lattice parameters and the space gather symmetry. Ultraviolet visible spectrometer (UV-visible) and Fourier transform infrared spectroscopy (FTIR) were utilized to characterize the optical properties of crystallite nanoparticles.

EXPERIMENTAL

In the synthesis of $\text{Co}_{1-x}\text{Cd}_x\text{Fe}_2\text{O}_4$ following chemicals were used without further purification. The chemicals *viz.*, $\text{Co}(\text{NO}_3)_2$, $\text{Cd}(\text{NO}_3)_2$, $\text{Fe}(\text{NO}_3)_3 \cdot 9\text{H}_2\text{O}$ and NaOH were procured from Merck. The deionized water is used throughout the experimental work.

Synthesis of spinel: The analytical grade used in preparation of CoCd ferrite ($\text{Co}_{1-x}\text{Cd}_x\text{Fe}_2\text{O}_4$) nanoparticles with structure ($x = 0.0, 0.2, 0.5$ and 0.8) was set up by the co-precipitation method. Fig. 1 demonstrates the synthesis flow-planner for nano-

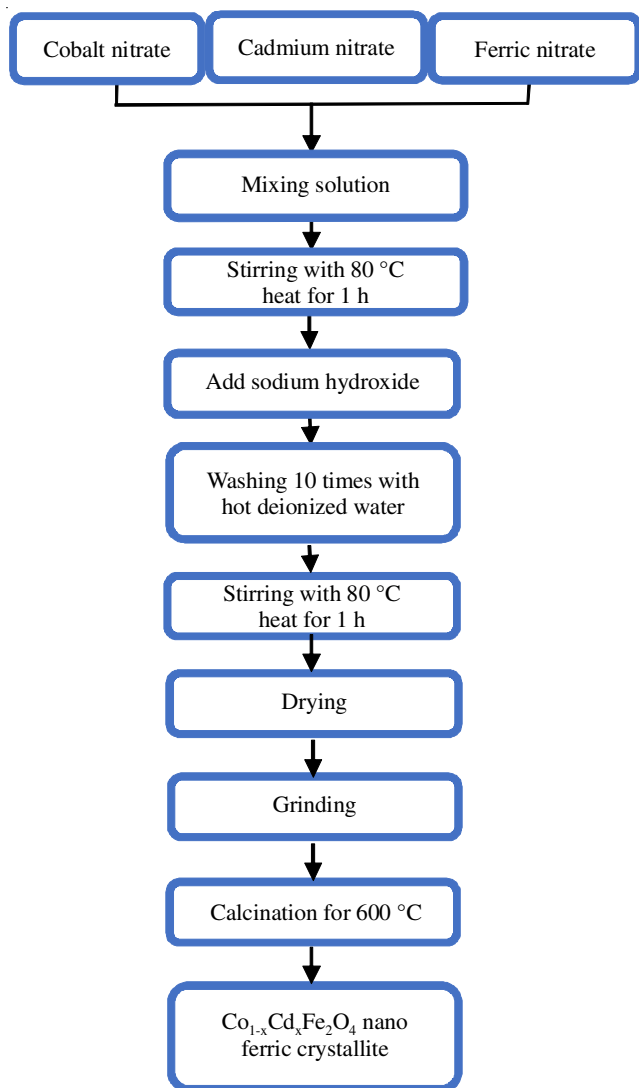


Fig. 1. Synthesis scheme for nanoparticles

particles generation. The solution of $\text{Fe}(\text{NO}_3)_3 \cdot 9\text{H}_2\text{O}$ (1 M, 25 mL), $\text{Co}(\text{NO}_3)_2$ (0.5 M, 25 mL) and $\text{Cd}(\text{NO}_3)_2$ were first blended and afterward slowly added NaOH (2 M, 25 mL) solution under stirring of 3000 rpm for 30 min to get a mixture of pH 11-13. The colloidal solution was then kept in a water bath at 80°C for 1 h to remove excess NaNO_3 from the powder. The precipitate was washed 10 times with hot deionized water until the filtrate had a pH 7 [16,17]. At that point, the samples were dried and ignition to absolute powder and more grounded to 600°C for 3 h in a temperature-controlled muffle heater Vulcan A-550 at a heating rate $10^\circ\text{C}/\text{min}$.

The X-ray investigation was performed to affirm to purity of the synthesized materials by Shimadzu 6000 X-ray diffractometer of a wavelength $\lambda = 0.15406$ nm source, FTIR spectroscopy (FTIR-8400S, Shimadzu), scanning electron microscopy (SEM), energy dispersive spectroscopy (EDS), atomic force microscope (AFM) and high-performance liquid chromatography (HPLC), while the assimilation of solution with various focus was calculated utilizing T80 UV/Vis spectrometer PG instruments.

RESULTS AND DISCUSSION

X-ray diffraction: To evaluate the crystal structure, the lattice section parameters and the space, a mass symmetry is significant in the investigation of structural, electrical and optical properties of ferrite nanoparticles. The results of single $\text{Co}_{1-x}\text{Cd}_x\text{Fe}_2\text{O}_4$ is affirmed in the wake of breaking down the X-ray diffraction pattern. The crystal structure is observed to be cubic with space gathering. Fig. 2 shows the X-ray diffraction pattern of $\text{Co}_{1-x}\text{Cd}_x\text{Fe}_2\text{O}_4$ nanoparticles having different composition ($x = 0.0, 0.2, 0.5$ and 0.8). The crystallite size, 2θ (deg) and FWHM (deg) are shown in Table-1. The crystal size is computed by utilizing the Debye-Scherrer's equation:

$$D = K \lambda / \beta \cos \theta$$

where D is the average particle size (nm), K is the dimension shape factor 0.9, λ is X-ray wavelength of $\text{CuK}\alpha$, β is the linear broadening at half the maximum intensity (radians) and θ is the Bragg angle.

Table-1 shows the average molecule size of nanocrystalline samples calculated from the XRD information utilizing Scherrer

No.	Samples	2θ ($^\circ$)	FWHM ($^\circ$)	Crystal size (nm)
1	CoFe_2O_4	35.5982	0.17310	58.98
		62.7759	0.22760	79.73
		57.1717	0.21000	72.91
2	CdFe_2O_4	34.1200	0.37860	26.48
		33.0099	0.30480	32.47
		35.6339	0.30930	34.19
3	$\text{Co}_{0.2}\text{Cd}_{0.8}\text{Fe}_2\text{O}_4$	33.0088	0.25780	38.38
		38.3017	0.26670	39.64
		55.2976	0.41670	34.97
4	$\text{Co}_{0.5}\text{Cd}_{0.5}\text{Fe}_2\text{O}_4$	33.0137	0.26060	37.98
		34.9723	0.55770	18.16
		38.3132	0.31280	33.82
5	$\text{Co}_{0.8}\text{Cd}_{0.2}\text{Fe}_2\text{O}_4$	35.1693	0.92330	21.98
		29.8435	0.80000	23.91
		62.0037	1.42000	24.89

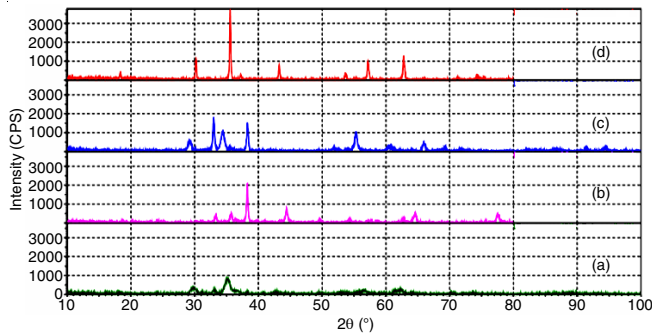


Fig. 2. X-ray patterns of $\text{Co}_{1-x}\text{Cd}_x\text{Fe}_2\text{O}_4$ nano-ferrites for (a) CoFe_2O_4 , (b) $\text{Co}_{0.2}\text{Cd}_{0.8}\text{Fe}_2\text{O}_4$, (c) $\text{Co}_{0.5}\text{Cd}_{0.5}\text{Fe}_2\text{O}_4$, (d) $\text{Co}_{0.8}\text{Cd}_{0.2}\text{Fe}_2\text{O}_4$

condition and found to be within the range (18.16-39.64 nm). The increased size with Cd^{2+} might be due to the fact that Cd^{2+} ions are bigger than Co^{2+} ions. Addition of Cd^{2+} at the detriment of Co^{2+} in the ferrite is expected to increase the lattice constant, which are smaller than (100 nm) in nanoscale [18].

Fig. 2 showed that CdFe_2O_4 is polycrystalline for cadmium and haematite (Fe_2O_4) by matching the patterns with the ASTM card by number 22-1063 (cadmium) and number 87-1164 (Fe_2O_4). From Fig. 2, it is also appeared that cadmium (Cd^{2+}) is higher than the ratio of haematite (Fe_2O_4).

FT-IR analysis: The infrared spectra of spinel $\text{Co}_{1-x}\text{Cd}_x\text{Fe}_2\text{O}_4$ with different ratio (0.2:0.8, 0.5:0.5, 0.8:0.2) with calcination temperatures 600°C were performed in the $4000\text{-}400\text{ cm}^{-1}$ range. The groups (ν_1 , ν_2) are observed in the range $1651.12\text{-}1506.46\text{ cm}^{-1}$ and $667.39\text{-}412.78\text{ cm}^{-1}$, separately. These groups are due to O-H extending vibration of free retained water and demonstrates the presence of hydroxyl groups in the synthesized ferrites [19,20]. The band (ν_3) for the samples are observed around 1651.12 cm^{-1} and is ascribed to the C=O extending vibration of carboxyl group. In range $1558.54\text{-}1506.46\text{ cm}^{-1}$, the band (ν_4) is due to extending vibration of nitrate group [21,22]. In the range of $800\text{-}400\text{ cm}^{-1}$, two principle ingestion groups with low intensity are seen around 412.78 and 667.39 cm^{-1} and might be is caused by metal oxygen vibration in the octahedral site. The ν_1 , ν_2 , ν_3 , ν_4 and ν_5 are retention groups around $1651.12\text{-}1558.54$, $1539.25\text{-}1506.46$, $615.31\text{-}590.24$ and $572.88\text{-}412.78\text{ cm}^{-1}$, respectively for the samples which are due to the vibration of tetrahedral and octahedral metal oxygen (M-O) groups in the lattices of combined nanocrystals.

Scanning electron microscopy (SEM): Fig. 3 shows the scanning electron micrographs of $\text{Co}_{1-x}\text{Cd}_x\text{Fe}_2\text{O}_4$ ($x = 0.0, 0.2, 0.5$ and 0.8). The grains are arbitrarily circulated and agglomerated. The particles are isolated as crystallite size increased due to substitution. The clearly separated porous bunch of Cd substituted CoFe_2O_4 are seen at 0.2 Cd doping having crystallite size of 39.64 nm. The porosity of this sample helps in keeping away from the distortion losses and also the isolated particle improves the transportation properties. Hence, substitution of Cd agglomeration becomes more because of the decrease in crystallite size.

Energy dispersive X-ray spectroscopy (EDS): The EDS analyses for coated Fe_2O_4 and spinel $\text{Co}_{1-x}\text{Cd}_x\text{Fe}_2\text{O}_4$ were performed. The EDS results are shown in Fig. 4.

Dielectric constant measurements: It can be seen from Fig. 5, the real and imaginary permittivity *versus* log frequency

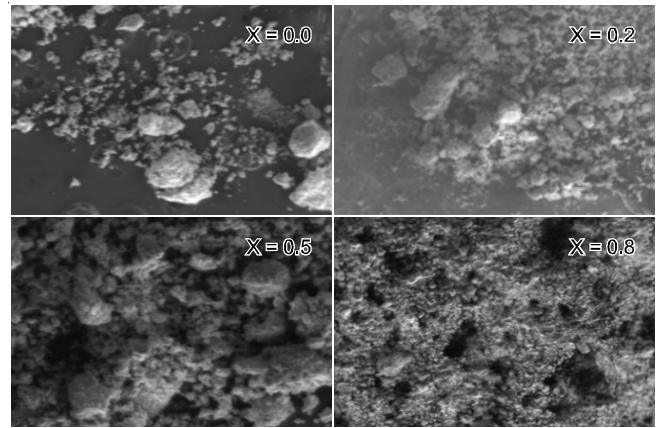


Fig. 3. SEM images of $\text{Co}_{1-x}\text{Cd}_x\text{Fe}_2\text{O}_4$ nano-ferrites for $x = 0.0, 0.2, 0.5$ and 0.8

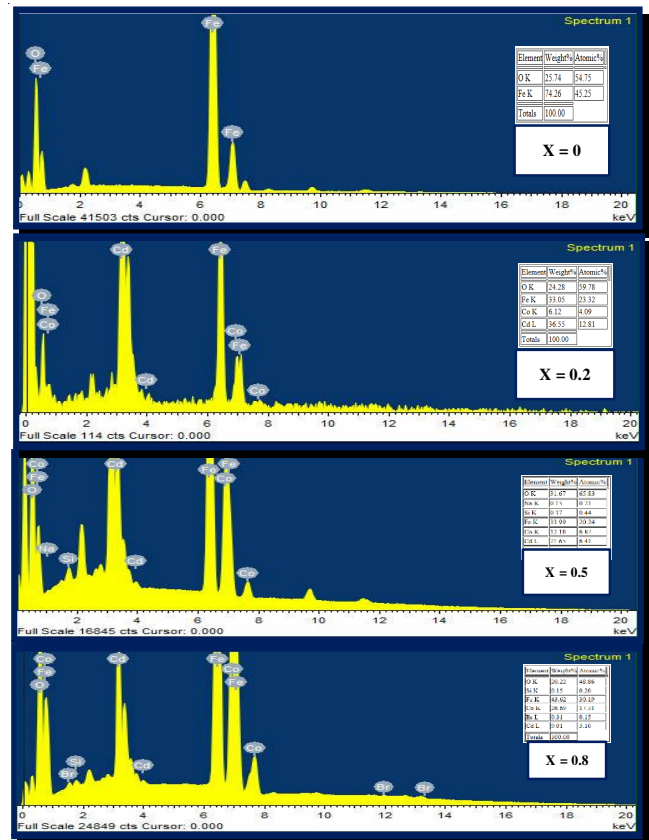


Fig. 4. EDS images of $\text{Co}_{1-x}\text{Cd}_x\text{Fe}_2\text{O}_4$ nano-ferrites for $x = 0.0, 0.2, 0.5$ and 0.8

of CoFe_2O_4 , individually, increase with decreasing frequency. The estimation performed at room temperature, subsequently, its effect on the permittivity activities can be disregarded.

The CoFe_2O_4 permittivity is represented by the quantify the orientable dipoles present in the framework and their capacity to situate under unapplied electric field. At low frequencies of applied voltage, all the free dipolar ions gathered in CoFe_2O_4 can fix themselves bringing about a higher permittivity esteem at these frequencies.

As the electric field frequency increases, the greater dipolar makes difficult to fix a distinguishable speed from the exchanging field, hence the commitments of these dipolar gathering to the permittivity continues diminishing bringing a persistently

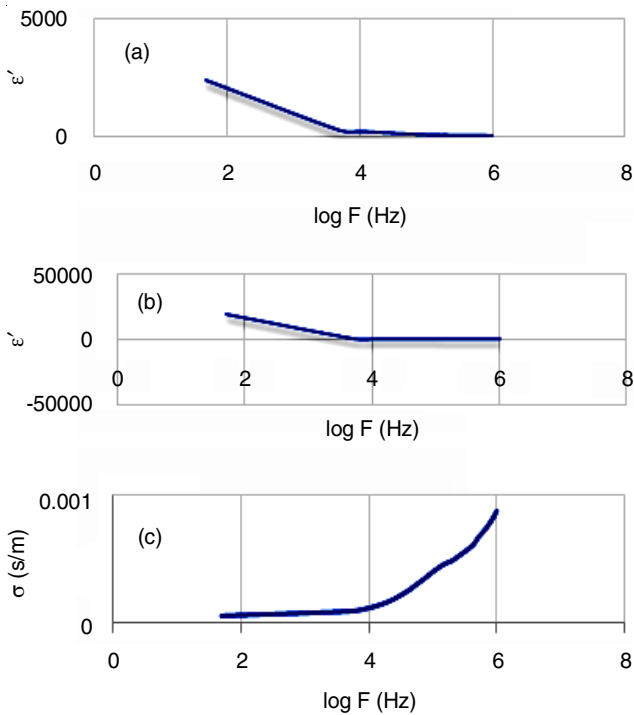


Fig. 5. Real permittivity (a), imaginary permittivity (b) and AC conductivity (c) versus log frequency for CoFe_2O_4

decreasing permittivity of CoFe_2O_4 system at higher frequencies [23]. The electrical conductivity relies upon the quantity of progress transporters and frequency of connected electric field on CoFe_2O_4 .

Electric measurements of spinel $\text{Co}_{1-x}\text{Cd}_x\text{Fe}_2\text{O}_4$ composites: Fig. 6 portrayed the variety of real part of dielectric permittivity (ϵ') with frequency for spinel $\text{Co}_{1-x}\text{Cd}_x\text{Fe}_2\text{O}_4$ composites, separately at room temperature. At low frequencies, permittivity reached higher qualities, in all cases, which decreased

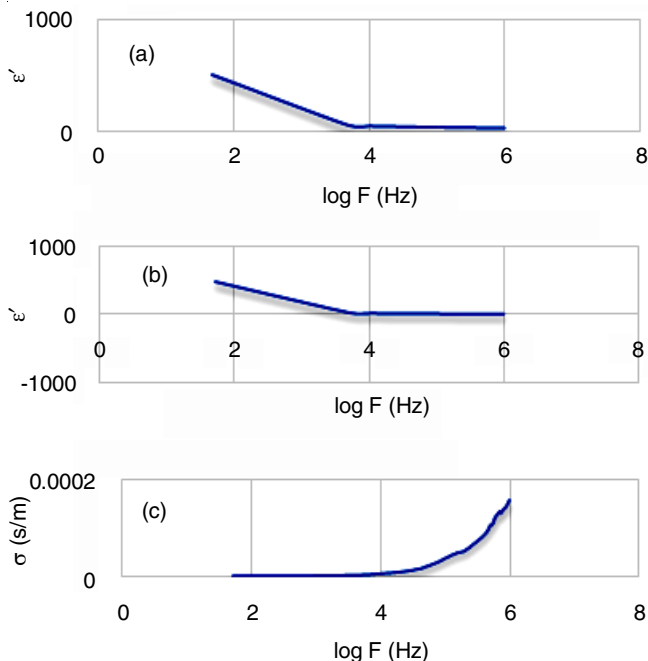


Fig. 6. Real permittivity, imaginary permittivity and AC conductivity versus log frequency for $\text{Co}_{0.5}\text{Cd}_{0.5}\text{Fe}_2\text{O}_4$

quickly with frequency expanding. This is sensible since at low frequency area, the rotation of field is moderate, giving therefore enough time to changeless and induced dipoles to adjust themselves in connection to the connected, prompting to upgraded polarization.

Improved estimations of dielectric permittivity (ϵ') particularly at low frequencies can be come back to interfacial polarization and/or anode polarization. Terminal polarization is related to the development of room changes at anode interfaces and depicted by high estimations of both real and imaginary part of dielectric permittivity [24,25].

Atomic force microscopy (AFM): Atomic force microscope (AFM) is a technique used to analyze the morphology of surface [26], which let us to see and measure structure of surface with high reliability and arrangement of individual atoms/molecules in the structure [27,28]. AFM depends on measuring the force between tip and surface of sample [29] (Fig. 7).

HPLC Chromatographic analyses: The course of photolysis process of spinel $\text{Co}_{1-x}\text{Cd}_x\text{Fe}_2\text{O}_4$ on phenol red surface was also monitored by HPLC chromatogram of spinel irradiation. Before irradiation, HPLC chromatogram showed the absorbance peak, which appeared at retention time of 3.34 min and after irradiation the intensity of this peak is gradually decreased with irradiation time.

Effect of spinel mass: Using different amount of catalyst (0.01, 0.1, 0.15, 0.2, 0.25 and 0.3 g), the effect on the photodegradation efficiency on phenol red was studied by taking different masses of catalyst ranged from 0 and 10 ppm of phenol red solution under UV light at 25 °C for 60 min. Fig. 8 showed that due to increased activity of $\text{Co}_{1-x}\text{Cd}_x\text{Fe}_2\text{O}_4$ results in the high efficient removal of phenol red. This may be protruded from the increase in the number of active sites available on the surface of catalyst for the reaction. For high amount of catalyst more than 0.2 g, photodegradation efficiency was decreased suitable to an agglomeration causing the increase particle size and decreased in particular surface area which leads to decrease in the quantity of surface dynamiclocales [30,31] as well high amounts of catalyst lead to increase of light diffusion. This tends to decrease the passing of irradiation through the sample. Therefore, the most effective photodegradation of $\text{Co}_{0.5}\text{Cd}_{0.5}\text{Fe}_2\text{O}_4$ was observed with 0.2 g of catalyst weight [32,33].

Effect of concentration of $\text{CoCdFe}_2\text{O}_4$: At different concentrations of $\text{Co}_{0.5}\text{Cd}_{0.5}\text{Fe}_2\text{O}_4$ (5, 10, 30, 50, 70 ppm) with 0.2 g of catalyst, the results showed an increase of photocatalytic degradation process when initial concentration of spinel $\text{Co}_{1-x}\text{Cd}_x\text{Fe}_2\text{O}_4$ increased because molecules of $\text{Co}_{0.5}\text{Cd}_{0.5}\text{Fe}_2\text{O}_4$ are photosensitive and when concentration increased more photons would be absorbed which lead to decreased deepness of light passage and low light transmittance [34,35]. As seen from Fig. 9, the optimum initial concentration of spinel $\text{Co}_{1-x}\text{Cd}_x\text{Fe}_2\text{O}_4$ is 10 ppm, because it results higher photocatalytic degradation than other concentrations of $\text{Co}_{0.5}\text{Cd}_{0.5}\text{Fe}_2\text{O}_4$.

Effect of temperature: The photocatalytic degradation rate of spinel using catalyst at different temperature ranging from 20 to 50 °C were investigated. Fig. 10 shows the effect of different temperatures on the photocatalytic degradation rate

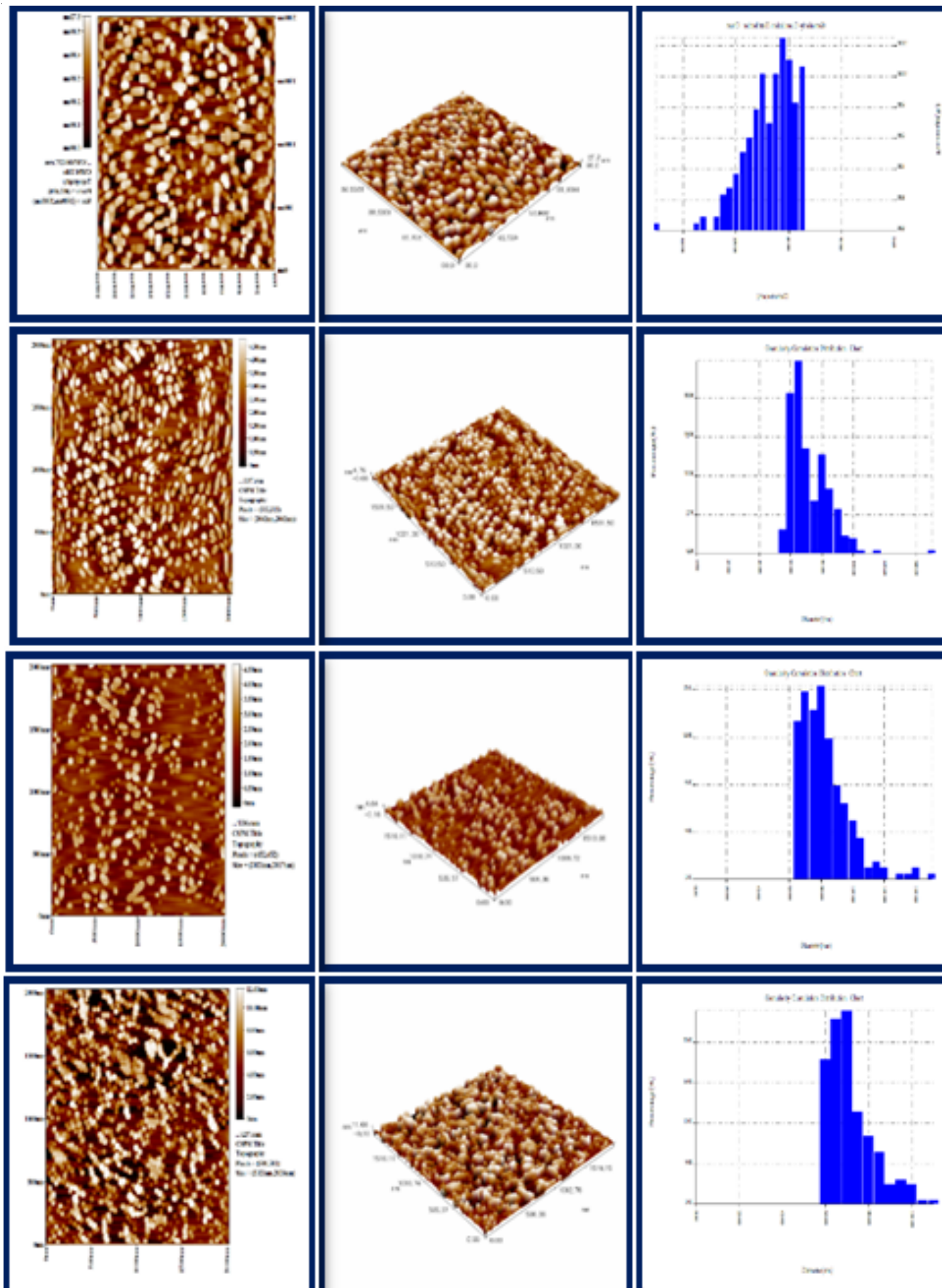
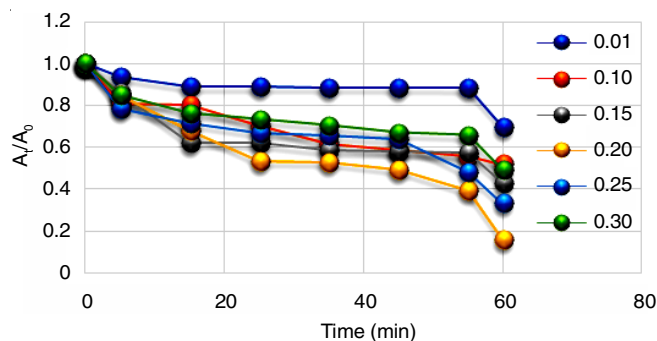
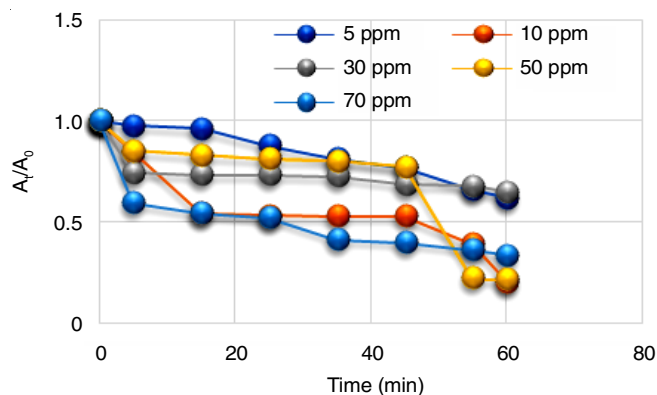
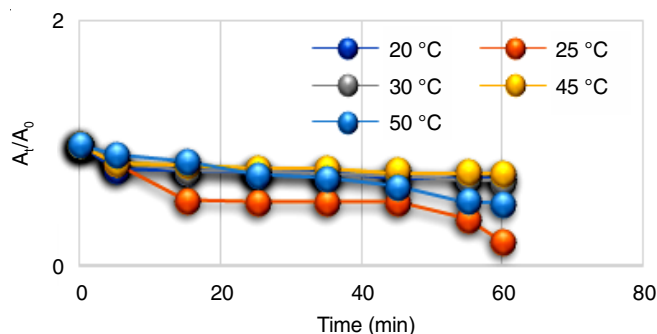


Fig. 7. AFM 2-D, 3-D and diameter images of (a) CoFe_2O_4 , (b) $\text{Co}_{0.2}\text{Cd}_{0.8}\text{Fe}_2\text{O}_4$, (c) $\text{Co}_{0.5}\text{Cd}_{0.5}\text{Fe}_2\text{O}_4$, (d) $\text{Co}_{0.8}\text{Cd}_{0.2}\text{Fe}_2\text{O}_4$

Fig. 8. Effect of the weight of spinel $\text{CoCdFe}_2\text{O}_4$ on photodegradationFig. 9. Effect of the concentration of $\text{Co}(\text{NO}_3)_2 \cdot 6\text{H}_2\text{O}$ Fig. 10. Change of (A_t/A_0) with irradiation time at different temperature

of spinel at a fixed initial concentration 10 ppm and 0.2 g $\text{Co}_{0.5}\text{Cd}_{0.5}\text{Fe}_2\text{O}_4$ catalyst. It is found that the photocatalytic degradation rate of spinel increases with temperature increase because increased temperature cause to increase generate free radicals and this lead to decrease in recombination process [36].

Effect of pH: The photocatalytic degradation rate of spinel is highly influenced by the value of pH of the reaction mixture. The photodegradation efficiencies of spinel with different pH values for reaction mixture are shown in Fig. 11. The degradation efficiency of the spinel was increased with increase in pH and the highest spinel degradation efficiency at pH 9. By increasing pH 11 of reaction mixture leads to decrease in photodegradation efficiency. The reduction in the removal efficiency of spinel at high pH values can be attributed due to the repulsion forces which are initiated between the negatively charged surface and the anionic groups present in spinel molecules. In addition to that decrease in the photocatalytic activity of spinel can be due to increase in the rate of recombination between (e^-/h^+) pairs [37].

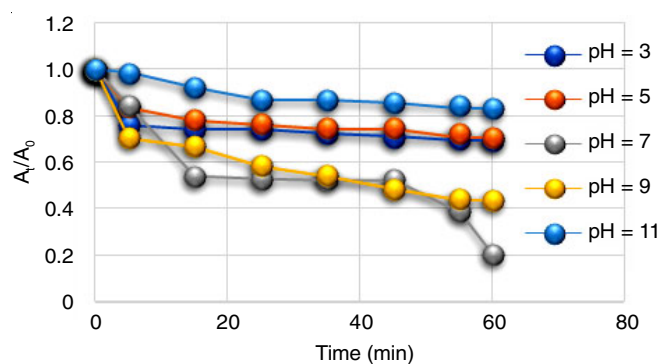


Fig. 11. Effect of pH

Conclusion

In this work, $\text{Co}_{1-x}\text{Cd}_x\text{Fe}_2\text{O}_4$ nanoparticles was prepared by co-precipitation method. The results showed that (0.5:0.5) ratio is more active than other ratio. The ability of spinel $\text{Co}_{1-x}\text{Cd}_x\text{Fe}_2\text{O}_4$ for photodegradation is achieved at 79.31 % at optimum condition of 0.2 g (spinel), concentration of salt 10 ppm, temperature 25 °C, pH 9 having radiation time of 60 min. The FT-IR spectra indicated two characteristic metal oxygen vibrational bands. The average particle size of nanoparticles are in the range of 18.16-39.64 nm as analyzed by XRD and EDS techniques. The dielectric constant and loss tangent δ decreases with frequency, whereas conductivity increases with increase in frequency.

CONFLICT OF INTEREST

The authors declare that there is no conflict of interests regarding the publication of this article.

REFERENCES

- Q. Xu, Y. Wei, Y. Liu, X. Ji, L. Yang and M. Gu, *Solid State Sci.*, **11**, 472 (2009); <https://doi.org/10.1016/j.solidstatesciences.2008.07.004>.
- M.B. Tian, *Magnetic Material*, Tsinghua University Press: Beijing (2001).
- A. Baykal, N. Kasapoglu, Y. Köseoglu, M.S. Toprak and H. Bayrakdar, *J. Alloys Compd.*, **464**, 514 (2008); <https://doi.org/10.1016/j.jallcom.2007.10.041>.
- A. Goldman, *Modern Ferrite Technology*, Marcel Dekker: New York (1993).
- A. Alarif, N.M. Deraz and S. Shaban, *J. Alloys Compd.*, **486**, 501 (2009); <https://doi.org/10.1016/j.jallcom.2009.06.192>.
- M. Flores-Acosta, M. Sotelo-Lerma, H. Arizpe-Chavez, F.F. Castillon-Barraza and R.J. Ramirez-Bon, *Solid State Commun.*, **128**, 407 (2003); <https://doi.org/10.1016/j.ssc.2003.09.008>.
- P. Pulisová, J. Kováč, A. Voigt and P. Raschman, *J. Magn. Magn. Mater.*, **341**, 93 (2013); <https://doi.org/10.1016/j.jmmm.2013.04.003>.
- M.Y. Lodhi, K. Mahmood, A. Mahmood, H. Malik, M.F. Warsi, I. Shakir, M. Asghar and M.A. Khan, *Curr. Appl. Phys.*, **14**, 716 (2014); <https://doi.org/10.1016/j.cap.2014.02.021>.
- L.S. Jan, S. Radiman, M.A. Siddig, S.V. Muniandy, M.A. Hamid and H.D. Jamali, *Colloids Surf. A Physicochem. Eng. Asp.*, **251**, 43 (2004); <https://doi.org/10.1016/j.colsurfa.2004.09.025>.
- D.S. Mathew and R.-S. Juang, *Chem. Eng. J.*, **129**, 51 (2007); <https://doi.org/10.1016/j.cej.2006.11.001>.
- S. Rahman, K. Nadeem, M. Anis-ur-Rehman, M. Mumtaz, S. Naeem and I. Letofsky-Papst, *Ceram. Int.*, **39**, 5235 (2013); <https://doi.org/10.1016/j.ceramint.2012.12.023>.
- A. Pradeep, P. Priyadharsini and G. Chandrasekaran, *J. Magn. Magn. Mater.*, **320**, 2774 (2008); <https://doi.org/10.1016/j.jmmm.2008.06.012>.
- N.N. Greenwood and A. Earnshaw, *Chemistry of the Elements*; Pergamon Press Ltd., Oxford, p. 279 (1984).

14. Y. Ichiyangi, M. Kubota, S. Moritake, Y. Kanazawa, T. Yamada and T. Uehashi, *J. Magn. Magn. Mater.*, **310**, 2378 (2007); <https://doi.org/10.1016/j.jmmm.2006.10.737>.
15. K.P. Thummer, M.C. Chhantbar, K.B. Modi, G.J. Baldha and H.H. Joshi, *J. Magn. Magn. Mater.*, **280**, 23 (2004); <https://doi.org/10.1016/j.jmmm.2004.02.017>.
16. M.I.M. Omer, A.A. Elbadawi and O.A. Yassin, *J. Appl. Ind. Sci.*, **1**, 20 (2013).
17. R. Ali, M.A. Khan, A. Mahmood, A.H. Chughtai, A. Sultan, M. Shahid, M. Ishaq and M.F. Warsi, *Ceram. Int.*, **40**, 3841 (2014); <https://doi.org/10.1016/j.ceramint.2013.08.024>.
18. V.K. Mittal, P. Chandramohan, S. Bera, M.P. Srinivasan, S. Velmurugan and S.V. Narasimhan, *Solid State Commun.*, **137**, 6 (2006); <https://doi.org/10.1016/j.ssc.2005.10.019>.
19. S. Dey, A. Roy, D. Das and J. Ghose, *J. Magn. Magn. Mater.*, **270**, 224 (2004); <https://doi.org/10.1016/j.jmmm.2003.08.024>.
20. P. Priyadharsini, A. Pradeep, P.S. Rao and G. Chandrasekaran, *Mater. Chem. Phys.*, **116**, 207 (2009); <https://doi.org/10.1016/j.matchemphys.2009.03.011>.
21. P.P. Hankare, R.P. Patil, A.V. Jadhav, R.S. Pandav, K.M. Garadkar, R. Sasikala and A.K. Tripathi, *J. Alloys Compd.*, **509**, 2160 (2011); <https://doi.org/10.1016/j.jallcom.2010.10.173>.
22. M.E. Sánchez-Vergara, J.C. Alonso-Huitron, A. Rodríguez-Gómez and J.N. Reider-Burstin, *Molecules*, **17**, 10000 (2012); <https://doi.org/10.3390/molecules170910000>.
23. K. Rahna, *Indian J. Eng. Mater. Sci.*, **13**, 62 (2006).
24. G.M. Tsangaris, G.C. Psarras and G.M. Tsangaris, *J. Mater. Sci.*, **33**, 2027 (1998); <https://doi.org/10.1023/A:1004398514901>.
25. G.C. Psarras, K.G. Gatos, P.K. Karahaliou, S.N. Georga, C.A. Krontiras and J. Karger-Kocsis, *Express Polym. Lett.*, **1**, 837 (2007); <https://doi.org/10.3144/expresspolymlett.2007.116>.
26. K. Chang, S. Cheng, Y. Chen, H. Huang and J. Liou, *J. Microbiol. Immunol. Infect.*, **46**, 405 (2013); <https://doi.org/10.1016/j.jmii.2012.08.004>.
27. P. West, Atomic Force Microscopy, United States by Oxford University Press Inc.: New York, edn 1 (2010).
28. M.J. Doktycz, C.J. Sullivan, P.R. Hoyt, D.A. Pelletier, S. Wu and D.P. Allison, *Ultramicroscopy*, **97**, 209 (2003); [https://doi.org/10.1016/S0304-3991\(03\)00045-7](https://doi.org/10.1016/S0304-3991(03)00045-7).
29. Y. Sugimoto, P. Pou, M. Abe, P. Jelinek, R. Perez, S. Morita and O. Custance, *Nature*, **446**, 64 (2007); <https://doi.org/10.1038/nature05530>.
30. Y. Ni, X. Ge, Z. Zhang, H. Liu, Z. Zhu and Q. Ye, *Mater. Res. Bull.*, **36**, 2383 (2001); [https://doi.org/10.1016/S0025-5408\(01\)00739-5](https://doi.org/10.1016/S0025-5408(01)00739-5).
31. S.J. Wilson, *J. Solid State Chem.*, **30**, 247 (1979); [https://doi.org/10.1016/0022-4596\(79\)90106-3](https://doi.org/10.1016/0022-4596(79)90106-3).
32. S. Kuboon and Y.H. Hu, *Ind. Eng. Chem. Res.*, **50**, 2015 (2011); <https://doi.org/10.1021/ie101249r>.
33. S. Thirumalairajan, K. Girija, N.Y. Hebalkar, D. Mangalaraj, C. Viswanathan and N. Ponpandian, *RSC Adv.*, **3**, 7549 (2013); <https://doi.org/10.1039/c3ra00006k>.
34. Y. Chen, Y. Zhang, C. Liu, A. Lu and W. Zhang, *Int. J. Photoenergy*, **Article ID 510158** (2012); <https://doi.org/10.1155/2012/510158>.
35. L. Yong, G. Zhanqi, J. Yuefei, H. Xiaobin, S. Cheng, Y. Shaogui, W. Lianhong, W. Qingeng and F. Die, *J. Hazard. Mater.*, **285**, 127 (2015); <https://doi.org/10.1016/j.jhazmat.2014.11.041>.
36. S. Ahmed, M.G. Rasul, R. Brown and M.A. Hashib, *J. Environ. Manage.*, **92**, 311 (2011); <https://doi.org/10.1016/j.jenvman.2010.08.028>.
37. L.-P. Zhu, G.-H. Liao, W.-Y. Huang, L.-L. Ma, Y. Yang, Y. Yu and S.-Y. Fu, *Mater. Sci. Eng.: B*, **163**, 194 (2009); <https://doi.org/10.1016/j.mseb.2009.05.021>.